






Liquid-liquid phase separation reduces radiative absorption by aged black carbon aerosols

Jian Zhang^{1,2,12}, Yuanyuan Wang^{1,12}, Xiaomi Teng¹, Lei Liu ¹, Yisheng Xu³, Lihong Ren³, Zongbo Shi ⁴, Yue Zhang⁵, Jingkun Jiang⁶, Dantong Liu¹, Min Hu⁷, Longyi Shao ⁸, Jianmin Chen⁹, Scot T. Martin ¹⁰, Xiaoye Zhang¹¹ & Weijun Li ^{1✉}

Black carbon aerosols absorb radiation and their absorptive strength is influenced by particle mixing structures and coating compositions. Liquid-liquid phase separation can move black carbon to organic particle coatings which affects absorptive capacity, but it is unclear which conditions favour this redistribution. Here we combine field observations, laboratory experiments, and transmission electron microscopy to demonstrate that liquid-liquid phase separation redistributes black carbon from inorganic particle cores to organic coatings under a wide range of relative humidity. We find that the ratio of organic coating thickness to black carbon size influences the redistribution. When the ratio is lower than 0.12, over 90% of black carbon is inside inorganic salt cores. However, when the ratio exceeds 0.24, most black carbon is redistributed to organic coatings, due to a change in its affinity for inorganic and organic phases. Using an optical calculation model, we estimate that black carbon redistribution reduces the absorption enhancement effect by 28–34%. We suggest that climate models assuming a core-shell particle structure probably overestimate radiative absorption of black carbon aerosols by approximately 18%.

¹Key Laboratory of Geoscience Big Data and Deep Resource of Zhejiang Province, Department of Atmospheric Sciences, School of Earth Sciences, Zhejiang University, Hangzhou, China. ²School of Environmental and Material Engineering, Yantai University, Yantai, China. ³State Key Laboratory of Environmental Criteria and Risk Assessment, Chinese Research Academy of Environmental Sciences, Beijing, China. ⁴School of Geography, Earth and Environmental Sciences, University of Birmingham, Birmingham, UK. ⁵Department of Atmospheric Sciences, Texas A&M University, College Station, TX, USA. ⁶State Key Joint Laboratory of Environment Simulation and Pollution Control, School of Environment, Tsinghua University, Beijing, China. ⁷State Key Joint Laboratory of Environment Simulation and Pollution Control, College of Environmental Sciences and Engineering, Peking University, Beijing, China. ⁸State Key Laboratory of Coal Resources and Safe Mining, China University of Mining and Technology, Beijing, China. ⁹Shanghai Key Laboratory of Atmospheric Particle Pollution and Prevention, Department of Environmental Science and Engineering, Fudan University, Shanghai, China. ¹⁰John A. Paulson School of Engineering and Applied Sciences, Harvard University, Cambridge, MA, USA. ¹¹Key Laboratory of Atmospheric Chemistry of CMA, Institute of Atmospheric Composition, Chinese Academy of Meteorological Sciences, Beijing, China. ¹²These authors contributed equally: Jian Zhang, Yuanyuan Wang. ✉email: liweijun@zju.edu.cn

Black carbon (BC), also often referred to soot (i.e., carbonaceous fractal-like aggregates), is an important type of light-absorbing aerosol particles^{1,2}. BC particles not only aggravate air pollution and pose significant health risks to the general public, but also they change atmospheric radiative forcing and influence global climate^{3–8}. Previous studies showed that the mixing structure of BC particles strongly influences their optical properties and their climate effects^{9–15}. For instance, when BC particles are coated by secondary aerosol components (e.g., nitrates, sulfates, and secondary organics), their light absorption enhances due to the “lensing effect”^{3,16}. However, the magnitude of the lensing effect remains highly uncertain due to the variations of coating materials and to the variable mixing structures between the BC and coatings^{15,17–19}.

To date, most aerosol instruments and climate models assume that internally mixed BC particles have core-shell structures^{3,10,20,21}, while such assumption alone could not adequately explain field-measured optical properties of BC particles^{22–24}. For instance, the difference between the absorption enhancement (E_{abs}) of observed BC in the atmosphere and modeled BC with the core-shell structure can reach ~14–150%^{4,16,25}. The deviation from the core-shell approximation can be largely attributed to the mixing state of BC and its distribution in individual particles^{17,26,27}, although the morphology of individual BC particle has an effect as well^{28–30}. Interestingly, a recent laboratory study suggested that the distribution of BC inside individual particles can change from the entire particle to the organic coating under the liquid-liquid phase separation (LLPS) of organic and inorganic species when the relative humidity (RH) was lower than 90%³¹. The movement of the position of BC in individual particles due to the LLPS has been called “BC redistribution”³¹. However, there is a lack of field data to support such statement. While some BC particles have so far been observed to distribute in organic coatings of individual particles in ambient environment using common electron microscopes^{32,33}, conditions favoring the distribution of BC particles within organic coatings are unclear and not elucidated.

The data from multiple field campaigns at two typical background sites and at an upwind urban site as well as laboratory experiments in this study support the finding showing the redistribution of BC from inorganic cores into organic coatings due to the LLPS. To our knowledge, this study is the first to provide the evidence of the redistribution of airborne BC particles from inorganic cores into organic coatings during the LLPS under a wide range of RH conditions using transmission electron microscopy (TEM) and cryogenic TEM (cryo-TEM) integrating with a humidity chamber. Moreover, a novel optical calculation model was further used to quantify the variation of BC optical absorption due to the BC redistribution induced by the LLPS.

Results and discussion

Mixing state and distribution of black carbon. Numerous aged BC particles with a wide size range of 40 nm to 1.5 μm were observed in both the rural and mountain background air in summer (Fig. 1 and Supplementary Figs. 1 and 2). Supplementary Figs. 3 and 4a show that the number fraction of BC-containing particles reached 44–47%, and the mass concentration of BC was $1.23 \pm 0.53 \mu\text{g m}^{-3}$ at the mountain site during the sampling period. Backward trajectory analysis indicates that these BC particles were mainly transported from upwind urban polluted areas (Supplementary Fig. 5).

BC-containing particles were classified into externally mixed and internally mixed particles (Fig. 1a). Supplementary Figs. 3 and 6a show that over 90% of BC particles were internally mixed with secondary aerosols in both the background and urban air.

These internally mixed BC-containing particles were normally formed through various aging processes including coagulation, condensation, and heterogeneous reactions among particle population or between particles and gases^{28,32,33}. To better obtain the mixing state of individual particles at one certain RH, the cryo-TEM integrating with a humidity chamber was applied to observe the ambient collected particles under the selected RH level (Supplementary Fig. 7). We found that individual secondary particles retained their phase separation (i.e., the core-shell structure) between organic matter and inorganic salts at $\leq 88\%$ RH (Figs. 1b and 2a and Supplementary Fig. 8a), which has been determined as LLPS^{34,35}. This RH probing result suggests that most of BC-containing secondary particles collected in the background air should be phase-separated because RH was often less than 88% during the field sampling periods (Supplementary Fig. 4a, b and Supplementary Table 1). We further obtained elemental profiles of C, S, and O across a typical secondary particle mixed with BC using the high-angle annular dark-field scanning TEM (HAADF-STEM). Figure 2a displays higher C, lower O, and extremely lower S in the organic coating compared to the inorganic salt core, further confirming the LLPS between the inorganic core and the organic coating. The finding is consistent with the conclusion from the recent studies that the phase-separated particles including the inorganic core and organic coating commonly occur in ambient air^{34,36}.

The distribution of BC inside the internally mixed particles was examined. TEM observations revealed two dominant types: BC in inorganic core (BC-in-Icore, BC occurring in S-rich particle) and BC in organic coating (BC-in-Ocoating, BC occurring in organic coating) (Fig. 1a). The cryo-TEM was further used to determine whether the distribution of BC was influenced by particle phase under $< 88\%$ RH. The cryo-TEM analysis showed that the distribution of BC inside individual BC-in-Ocoating particles did not change at 75 and 86% RH when these particles changed from the solid phase to the liquid phase (Fig. 1b). However, we noticed that BC particles tended to move from the edge of individual secondary particles towards the center following the disappearance of the LLPS at $> 88\%$ RH (Fig. 1b). These observations suggest that the phase change of secondary aerosols do not affect the distribution of BC inside the particles when these BC-containing particles remain LLPS. As a result, the dry state of the phase-separated BC-containing particles observed by the TEM can represent the distribution of BC inside individual particles with the LLPS in the ambient air.

The number fractions of BC-in-Icore and BC-in-Ocoating particles were counted in 2080 BC-containing particles. Figure 2b shows that BC-in-Ocoating particles were dominant, accounting for 54–64% with an average of 59% (25 samples in total) in the background air. However, BC-in-Icore particles were dominant, accounting for 88% by number in all the BC-containing particles at the upwind urban site (Supplementary Fig. 6a). Moreover, we found that 75% of BC particles were embedded in secondary particles with LLPS in the background air but only 32% in the urban air (Fig. 2b and Supplementary Fig. 6a). These results indicate that BC particles tend to redistribute from inorganic salt cores into organic coatings with the increase of organic matter because individual secondary particles often contain more organics following particle transport from urban to background air³⁶. Although aerosol condensation and coagulation might directly cause some BC particles to mix into organic coatings in the air³³, the significant change in the distribution of BC inside individual particles from urban to background air reflected that the BC redistribution was the major process to form abundant BC-in-Ocoating particles. In the following sections, we further quantified how the LLPS affects the distribution of BC inside individual particles.

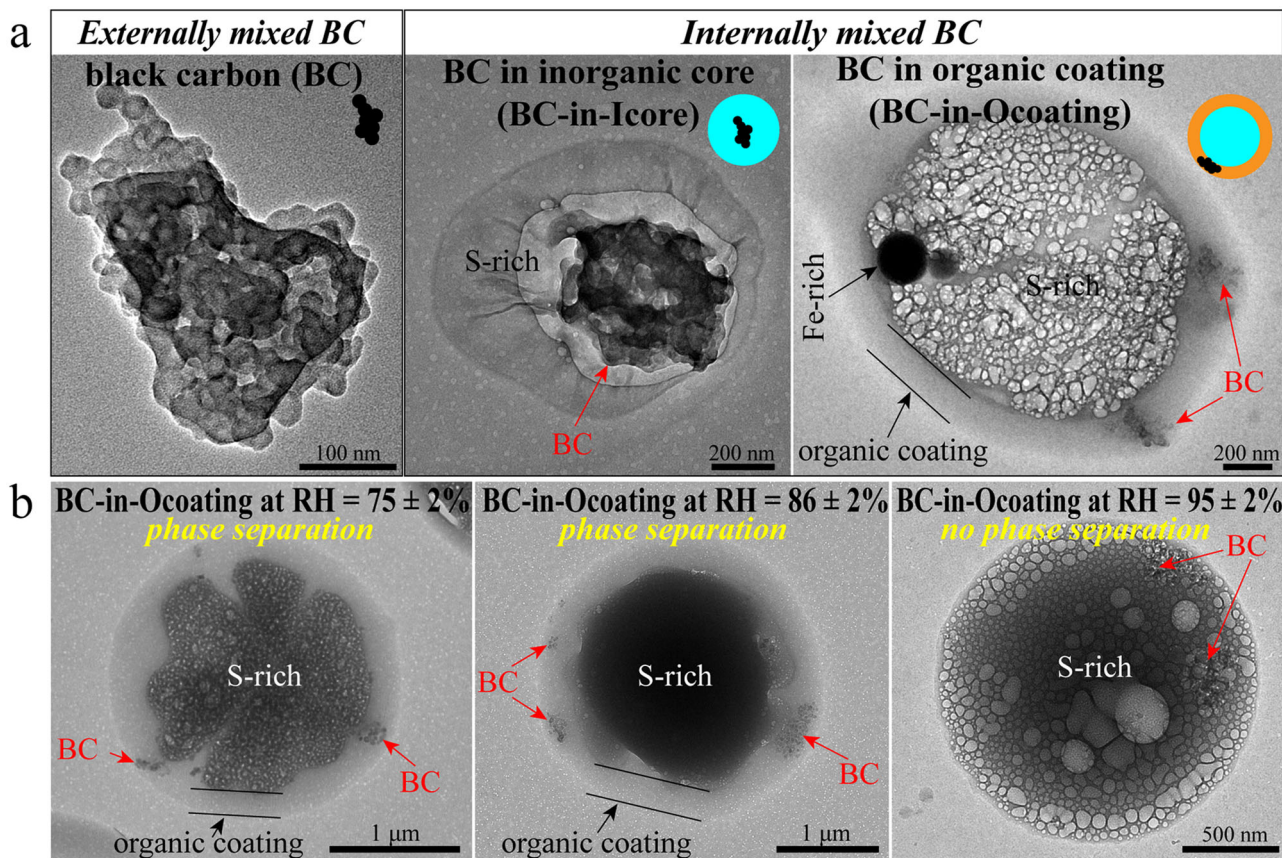


Fig. 1 Typical transmission electron microscopy (TEM) and cryogenic TEM (cryo-TEM) images of black carbon (BC)-containing particles with different mixing structures. **a** TEM images of externally mixed BC particle, BC in S-rich (BC-in-Icore) particle, and BC in organic coating (BC-in-Ocoating) particle. The mixing models of BC-containing particles are shown in the upper right corners of the TEM images. The black circle aggregates, cyan circles, and orange rings represent BC, S-rich, and organic coatings, respectively. **b** Cryo-TEM images of BC-in-Ocoating particles. These particles were exposed to atmospheric conditions with different relative humidity (RH) = 75 ± 2%, 86 ± 2%, and 95 ± 2% for 10 min before being frozen, respectively. The BC-in-Ocoating particles at RH of 75 ± 2% and 86 ± 2% remained liquid-liquid phase separation (LLPS) between organic matter and inorganic salts. The LLPS of the BC-in-Ocoating particle disappeared when it was at 95 ± 2% RH.

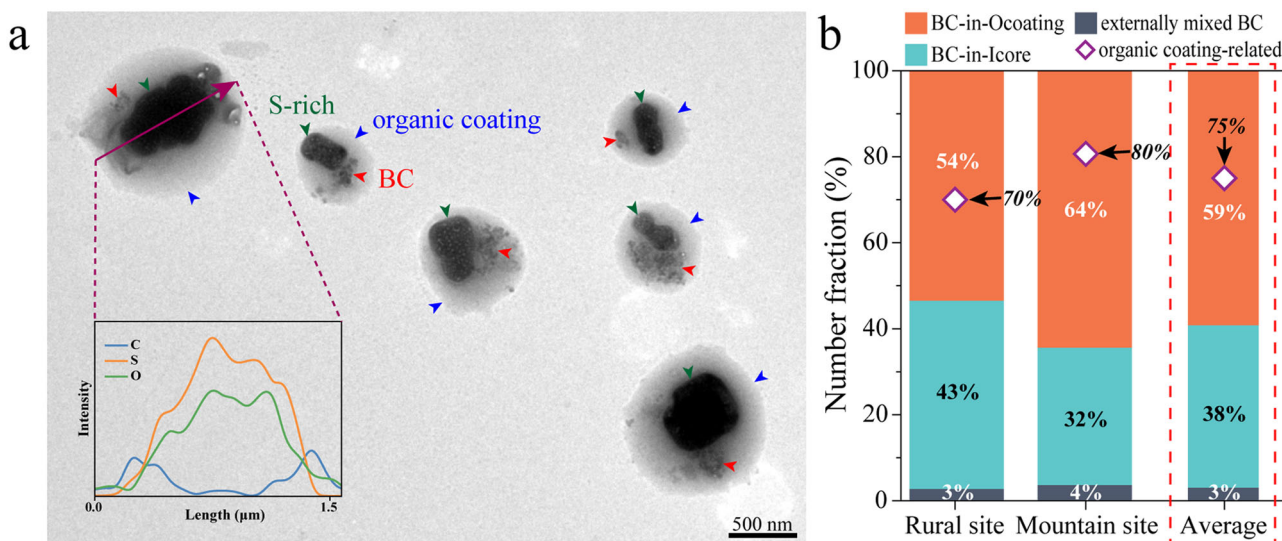


Fig. 2 Distribution of BC inside individual particles and number fractions of BC particles in the background air. **a** A typical TEM image of BC-in-Ocoating particles in the background air at low magnification. The red, green, and blue arrows indicate BC, S-rich particles, and organic coatings. Line scanning of a typical secondary particle with organic coating by the high-angle annular dark-field scanning TEM (HAADF-STEM) shows elemental profiles of C, S, and O across the particle. **b** Number fractions of BC particles with different distributions of BC at two background sites. The purple diamonds indicate individual BC-containing particles with the LLPS.

Organic coating thicknesses and size distribution of BC-containing particles. Further analysis established that the distribution of BC inside individual particles is related to two parameters: the organic coating thickness (T_{OC}) and the BC diameter (D_{BC}). Figure 3a shows that the number fraction of BC-in-Ocoating particles is strongly correlated with T_{OC} with $R^2=0.69$ in the background air. When T_{OC} is thinner than 80 nm measured by TEM and atomic force microscopy (AFM), BC-in-Icore particles are dominant, accounting for 63% of all BC-containing particles (Fig. 3a). When T_{OC} is thicker than 80 nm, BC-in-Ocoating particles become the dominant type, reaching an average of 64% by number (Fig. 3a). This variation suggests that the distribution of BC inside individual particles changes from being in inorganic salt cores to organic coatings when organic coatings become thicker. In some cases, two or more BC inclusions occur in organic coatings of individual particles. For example, Fig. 3b shows four tiny BC particles in the organic coating. The percentage of BC-in-Ocoating particles containing multiple BC ($N > 1$) in all the BC-in-Ocoating particles increases from $25 \pm 7\%$ to $52 \pm 15\%$ following an increase in T_{OC} from 62 ± 13 nm to 98 ± 10 nm (Fig. 3a). Figure 3c further shows that the average T_{OC} of BC-in-Ocoating particles is 87 nm in the background air, which is significantly greater than 47 nm for the BC-in-Icore particles. In the urban air, the average T_{OC} of BC-in-

Icore particles is only 30 nm (Supplementary Fig. 6b). These results suggest that T_{OC} may have a major impact on the distribution of BC inside individual particles.

Figure 3d displays the number fractions of BC-in-Icore and BC-in-Ocoating particles collected in the background air among different BC diameter (D_{BC}) bins from 40 nm to 1500 nm. We found that the number fractions of BC-in-Icore and BC-in-Ocoating particles vary inversely with the change of D_{BC} (Fig. 3d). The number fraction of BC-in-Icore particles increases from 23 to 63% with an increase in D_{BC} from 40–240 nm to 240–1500 nm, but the number fraction of the BC-in-Ocoating particles decreases from 67 to 31% (Fig. 3d). The result suggests that finer BC particles favor distribution into organic coatings compared to coarser ones. Therefore, D_{BC} also affects the distribution of BC inside individual particles. Moreover, all BC particles with $D_{BC} > 1000$ nm distribute into inorganic salt cores in internally mixed particles (Fig. 3d), suggesting that the D_{BC} range should be constrained to less than 1000 nm when considering the variation of the distribution of BC inside individual particles.

The above data show that T_{OC} and D_{BC} have crucial influences on the distribution of BC inside the phase-separated particles. It is well known that the size of BC is less prone to change during its aging, unless becoming more compact²⁸. However, T_{OC} can continuously increase following particle aging during their long-

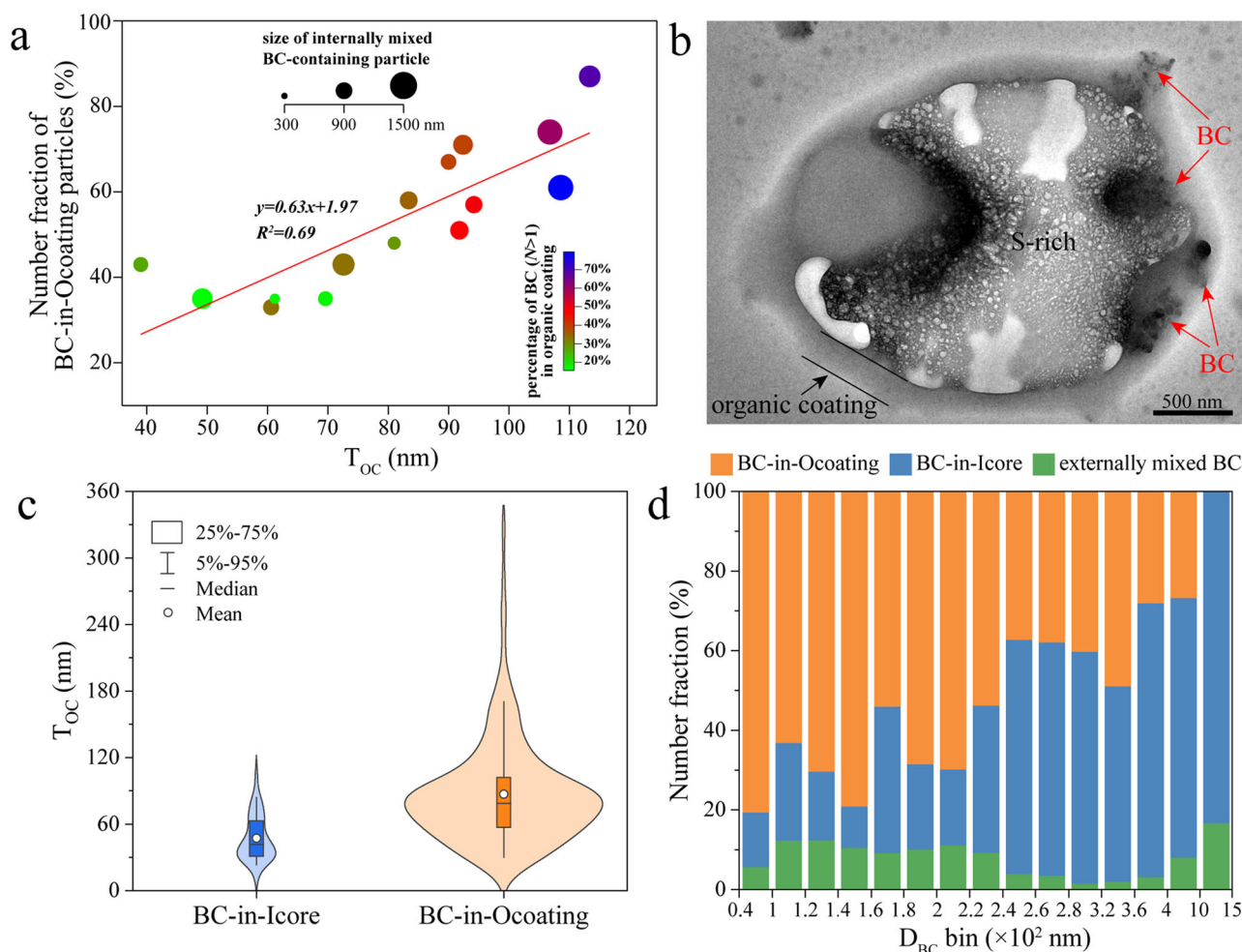


Fig. 3 Organic coating thickness (T_{OC}) and size distribution of BC within individual particles in the background air. **a** Correlation between T_{OC} and number fraction of BC-in-Ocoating particles in internally mixed BC-containing particles. The color bar represents the percentage of BC-in-Ocoating particles containing multiple BC in all the BC-in-Ocoating particles. **b** A typical TEM image of BC-in-Ocoating particle containing four tiny BC particles. **c** T_{OC} of BC-in-Icore and BC-in-Ocoating particles. The blue and orange shadows represent the distribution of the T_{OC} data. **d** Number fractions of BC-in-Ocoating, BC-in-Icore, and externally mixed BC particles in different BC diameter (D_{BC}) bins from 40 nm to 1500 nm.

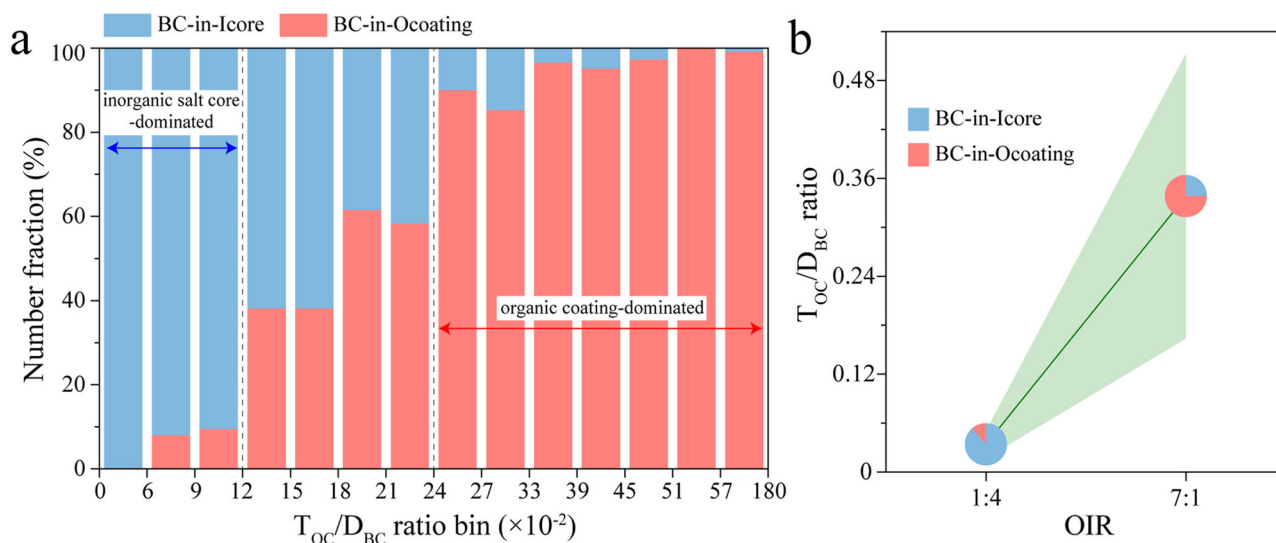


Fig. 4 Distribution of BC inside individual particles depending on the ratio of T_{OC}/D_{BC} . **a** Variation in the number fractions of field-observed BC-in-Icore and BC-in-Ocoating particles from the T_{OC}/D_{BC} ratio bins of 0–1.8. **b** Comparisons on the BC distribution and the T_{OC}/D_{BC} ratio of organic/inorganic/BC mixed particles generated from the suspensions with organic-to-inorganic dry mass ratio (OIR) = 1:4 and OIR = 7:1 in the laboratory. The green shadow indicates the standard deviation of the T_{OC}/D_{BC} ratio.

range transport³⁶. Therefore, it is necessary to consider the relationship between T_{OC} and D_{BC} during the redistribution of BC inside individual particles.

Here we propose a new parameter (i.e., the ratio of T_{OC}/D_{BC}) to investigate the redistribution of BC particles inside individual particles. Figure 4a shows that the distribution of BC inside individual particles is strongly correlated with the T_{OC}/D_{BC} ratio. When the T_{OC}/D_{BC} ratio is lower than 0.12, over 90% of BC particles distribute in inorganic salt cores (Fig. 4a). However, nearly all the BC particles are redistributed into organic coatings whenever the T_{OC}/D_{BC} ratio exceeds 0.24 (Fig. 4a). In addition to the T_{OC}/D_{BC} ratio, the cryo-TEM observations show that the distribution of BC particles is also dependent on RH, as the position of BC tends to approach the center of individual secondary particles following the disappearance of the LLPS at > 88% RH (i.e., T_{OC}/D_{BC} ratio = 0) (Fig. 1b and Supplementary Fig. 8b). Li et al.³⁷ showed that the organic coating only contributes less than 10% of the growth factor of individual secondary particles at \leq 88% RH. This suggests that the change of T_{OC} is limited with the variation of the particle phase at \leq 88% RH. Therefore, the lower RH at \leq 88% has a little effect on T_{OC} , but the higher RH at > 88% that leads to the disappearance of LLPS of particles can influence the distribution of BC inside individual particles.

Laboratory evidence and possible mechanisms for BC redistribution. To further confirm the redistribution of BC from inorganic cores into organic coatings and its dependence on the T_{OC}/D_{BC} ratio, we performed a laboratory experiment to observe the distribution of BC inside individual particles. These individual BC-containing particles were generated from two organic/inorganic/BC mixed suspensions with organic-to-inorganic dry mass ratios (OIRs) of 1:4 and 7:1 (Supplementary Fig. 9). The laboratory results show that the BC-containing particles dominated by BC-in-Ocoating particles have higher T_{OC} (93 nm) than those dominated by BC-in-Icore particles (17 nm) (Fig. 4b and Supplementary Fig. 10). Moreover, the dominant type of the laboratory-generated BC-containing particles changes from BC-in-Icore particles to BC-in-Ocoating particles when the T_{OC}/D_{BC} ratio increases from 0.04 to 0.34 (Fig. 4b), supporting the

observations for the ambient particles shown in Fig. 4a. By combining the data from both laboratory and field measurements, we conclude that the LLPS of secondary organic/inorganic mixed particles can facilitate BC redistribution into the organic coating from the inorganic salt core with the T_{OC}/D_{BC} ratio exceeding 0.24.

Based on TEM-EDS analysis, we estimated O/C ratios of organic coatings at 0.43 ± 0.06 in the background air (Supplementary Fig. 11), suggesting that organic matter in the coating had relatively low polarity³⁸. Previous studies showed that BC particles contained saturated and unsaturated hydrocarbons, polycyclic aromatic hydrocarbons (PAHs), and partially oxidized organics through the organic condensation^{39–42}. Buseck et al.⁴³ demonstrated that BC particles have organic coatings of several nanometers thickness by using the high-resolution TEM. Therefore, the aggregated carbonaceous spheres more or less contain organic matter (Fig. 1a, externally mixed BC), which can form an organic surface with a certain polarity on BC through aging^{44,45}. These organic species on BC particles have a higher affinity toward secondary organic aerosol coatings than to inorganic salts due to the intermolecular forces and interactions between similar chemical bonds³¹, which induces BC movement and redistribution within individual particles. We found larger T_{OC} values in BC-in-Ocoating particles than in BC-in-Icore particles (Fig. 3c), implying that thicker organic coatings on BC-in-Ocoating particles have larger volumes to cover BC and contribute to its movement following the LLPS compared to BC-in-Icore particles. This may be the reason to why fine BC particles (< 1000 nm) tend to move into organic coatings from inorganic salts following the increase in T_{OC} (Fig. 3a and Supplementary Figs. 8b and 10).

Reduced radiative absorption by BC redistribution. The variation of the distribution of BC in individual particles effectively changes its optical properties such as E_{abs} ^{11,18,26,31,46}. Here, a novel Electron-Microscope-to-BC-Simulation (EMBS) tool developed by Wang et al.²⁴ was further utilized to combine with the Discrete Dipole Approximation (DDA) for the optical calculations of aged BC particles. Based on the distribution of BC inside individual secondary particles, we determined three types of internally mixed BC particles (BC-in-Icore without organic

coating (basic core-shell model), BC-in-Icore with organic coating (phase-separated core-shell model), and BC-in-Ocoating (redistributed model)) to calculate their E_{abs} relative to the BC core at 550 nm (Fig. 5a, b). The basic core-shell model and phase-separated core-shell model were further classified into two types, respectively. Figure 5a, b displays their mixing structures: BC in the center and in the eccentric area of individual particles for the basic core-shell model and BC in the center and touching the interface between the organic and inorganic species for the phase-separated core-shell model. The models containing one and two BC particles were considered in the optical calculation due to their dominance in BC-containing particles (Supplementary Fig. 12). In this study, organic coatings were assumed to be non-absorbing with the refractive index of $1.65 + 0i$ ⁴⁷.

The E_{abs} of the basic core-shell model is 2.35–2.44 at 550 nm, which is slightly lower than 2.57–2.64 of the phase-separated core-shell model with T_{OC} at 80–81 nm (Fig. 5b and Supplementary Fig. 13). This suggests that non-absorbing organic coatings have a little effect on the light absorption of the basic core-shell model. When we change the distribution of BC particles from the inorganic core to the organic coating, the E_{abs} significantly decreases from 2.57–2.64 for the phase-separated

core-shell model to 1.75–1.86 for the redistributed model (Fig. 5b). This implies that the optical absorption of the redistributed model reduces by 28–34% compared to the phase-separated core-shell model, which is higher than the reported 20–30% decrease following BC movement from the center to the edge of water droplets or organic aerosols^{26,46}. On the contrary, Brunamonti et al.³¹ calculated increased E_{abs} from redistributed BC particles compared to core-shell BC particles. This reverse result should be ascribed to the inappropriate model of redistributed BC particles used in that study which assumed BC particles to be the shell and inorganic salts to be the core. The adopted redistributed BC model is totally different from aged BC particles in the ambient air as shown in Figs. 1 and 2a. Based on the above comparisons, we confirm that our calculated E_{abs} of BC-containing particles is credible because EMBS combined with DDA can consider various complicated mixing structures of BC particles and calculate their optical parameters (see methods). It should be noted that the E_{abs} for BC in the eccentric area is 1.89–2.22 in the basic core-shell model and for BC touching the interface between the organic and inorganic species is 2.38–2.61 in the phase-separated core-shell model (Supplementary Table 2). These two E_{abs} results are lower than 2.66–2.81 and 2.67–2.76 for BC in the center in the above

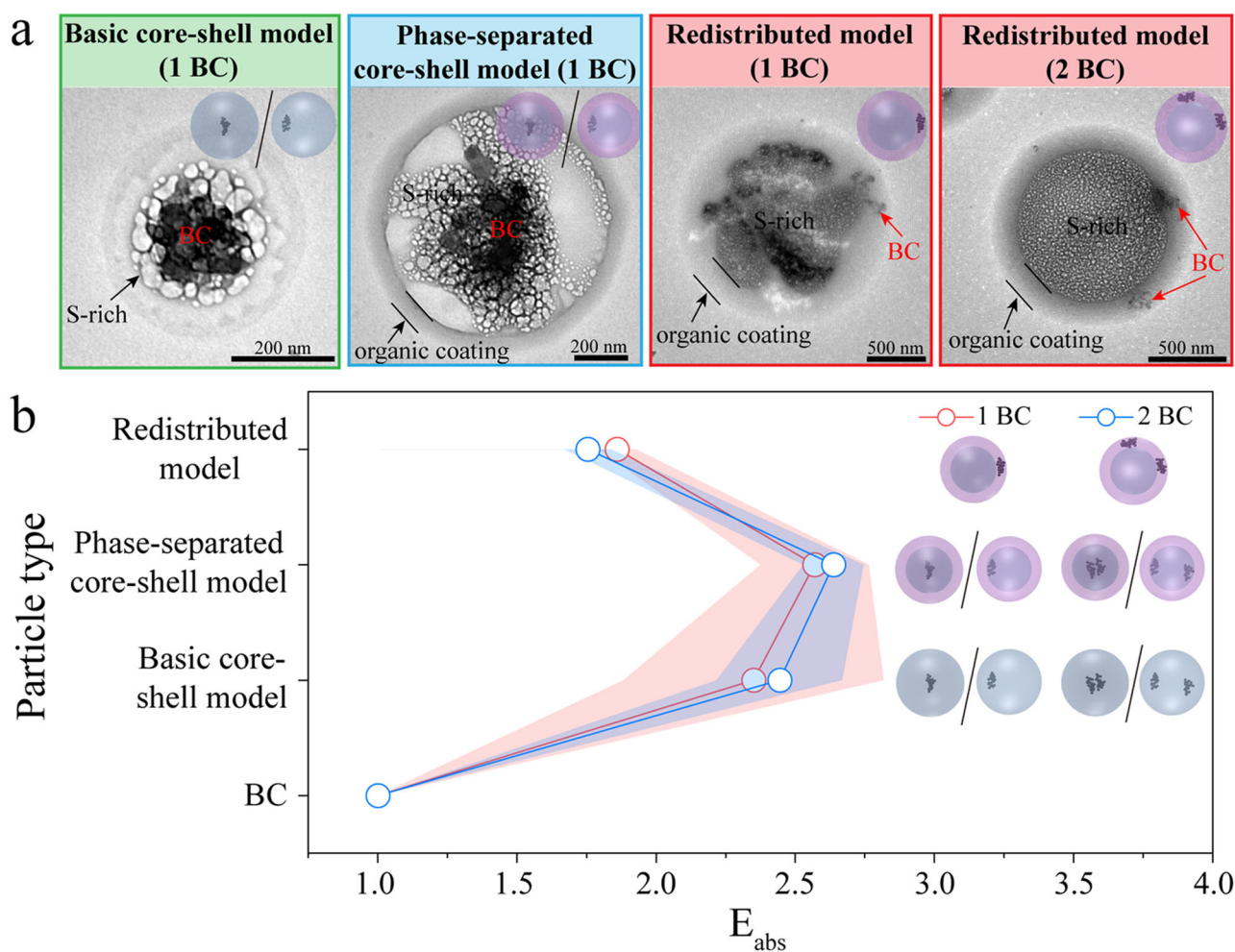


Fig. 5 Light absorption enhancement of BC-in-Icore and BC-in-Ocoating particles. **a** Three types of internally mixed BC particles (BC-in-Icore without organic coating (basic core-shell model), BC-in-Icore with organic coating (phase-separated core-shell model), and BC-in-Ocoating (redistributed model)) containing one or two BC particles with their models in the upper right corners. The basic core-shell model includes two types: BC in the center and in the eccentric area of individual particles. The phase-separated core-shell model also includes two types: BC in the center and touching the interface between the organic and inorganic phases of individual particles. **b** Absorption enhancement (E_{abs}) of the basic core-shell model, phase-separated core-shell model, and redistributed model containing one and two BC particles. The organic coating is assumed to be the non-absorbing organic aerosol. The red and blue shadows indicate the standard deviation of the E_{abs} .

two models but still higher than 1.75–1.86 for the redistributed model (Supplementary Table 2). Therefore, we can conclude that the radiative absorption of BC particles largely depends on the position of BC in individual particles.

Supplementary Fig. 12 shows that the redistributed BC particles account for 59% by number in BC-containing particles in the background air. If we consider the real mixing structure of BC-containing particles instead of only the core-shell structure, the deviation of radiative absorption of BC between the real mixing structure and the core-shell structure can be estimated in the background air. Based on the E_{abs} (Fig. 5b) and the fraction of BC-containing particles with different mixing models (Supplementary Fig. 12), we finally obtained that the radiative absorption of BC in the background air is overestimated by ~18% in previous optical models (Fig. 6) which assume all internally mixed BC particles to be the core-shell model^{3,10,48}. The above findings highlight the new insight into BC redistribution due to the LLPS of secondary organic and inorganic species and suggest the reduction of BC radiative absorption caused by the BC redistribution. In view of the prevalence of LLPS in urban and background air, atmospheric aerosols and climate models should account for the BC redistribution phenomenon to improve the current BC-mixing models and climate predictions.

Methods

Observation sites and sample collection. Three field campaigns were conducted: at an urban site (Beijing city (39.98° N, 116.33° E)) from 2 to 15 June 2013, at a rural site (Yucheng Integrated Agricultural Experimental Station (36.95° N, 116.60° E)) from 1 to 17 June 2013, and at a mountain site (Wudang Mountain Station (32.40° N, 111.04° E, 862 m above sea level)) from 13 to 23 June 2018, respectively (Supplementary Fig. 1). The rural and mountain sites are typical background air quality monitoring stations in northern and central China. The urban site is in one of the upwind areas of the rural background site (Supplementary Fig. 5a).

Individual aerosol particles at three sampling sites were collected on transmission electron microscopy (TEM) grids and silicon wafers using individual particle samplers equipped with the single-stage cascade impactor of 0.5 mm jet

nozzle (Genstar Inc., China). These particles were collected at local time of 02:00–03:00, 08:00–10:00, 13:00–15:00, and 17:00–20:00 and the volume flow was 1 L min⁻¹. To prevent particles overlapping on the substrates of TEM grids and silicon wafers, the sampling durations were controlled between 10 s and 30 s at the urban and rural sites and 10 min to 30 min at the mountain site according to ambient PM_{2.5} mass concentrations. Supplementary Table 1 shows the collected information of individual particle samples. After collecting individual particles, we stored samples in dry (relative humidity (RH): ~20%), clean, and airtight containers for next laboratory analyses.

Mass concentrations of black carbon (BC) at the mountain site were obtained using an Aethalometer AE-31 instrument (Magee Scientific, USA, 5 L min⁻¹). Details can be found in Xu et al.⁴⁹. PM_{2.5} concentrations and RH at the mountain site were obtained from the Wudang Mountain Station. RH at the rural and urban sites was measured from automated weather meters (GRWS100, USA).

Microscopic analyses. A total of 400 individual particles in eight samples at the urban site, 1165 individual particles in 13 samples at the rural site, and 3095 individual particles in 12 samples at the mountain site were analyzed using TEM (JEM-2100, JEOL, Japan) with energy-dispersive X-ray spectrometry (EDS, Oxford Instruments, U.K.). TEM can present physical characteristics (e.g., morphology and mixing state) of individual particles, and EDS provides chemical information (e.g., elemental composition and weight ratio of elements). Cu element is not considered in this study as TEM grids are made of Cu. Because the distribution of collected individual particles in TEM grids presented coarser particles in the sampling center and finer particles on the periphery, five areas from the sampling center to periphery were selected to observe individual particles. The high-angle annular dark-field scanning TEM (HAADF-STEM) was further employed to obtain the elemental profiles of particles, which can indicate the core-shell structure. Moreover, the equivalent circle diameters (ECDs), areas, and perimeters of particles were measured using a TEM image analysis software (Radius, EMSIS GmbH, Germany). The classification of individual particles is described in detail in Supplementary Text 1.

Because individual particle samples were dried during storage under ~20% RH, the common TEM can only obtain morphology of dry particles and cannot well observe semi-volatile aerosol components. The integration of cryogenic TEM (cryo-TEM) (Talos F200C, FEI, The Netherlands) and a vitrobot mark IV humidity chamber (FEI, The Netherlands) was employed to simulate the real mixing structure of individual particles under different RH (Supplementary Fig. 7). It is well known that cryo-TEM analysis with the low temperature at ~104 K can exclude the possible effect of water evaporation and the sublimation of some secondary inorganic salts and organics under vacuum on the mixing state of individual particles, including the distribution of BC³⁶. To restore phase states of individual particles in the ambient atmosphere, each sample was put into the

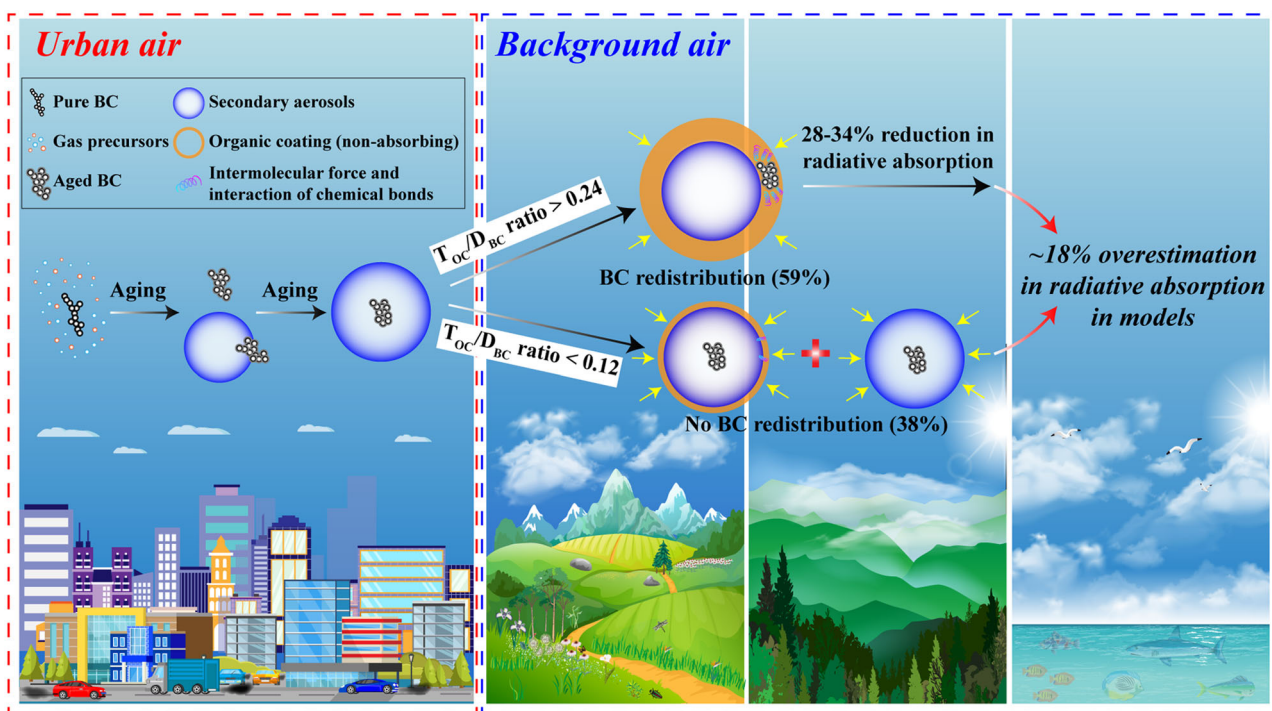


Fig. 6 A schematic diagram of BC redistribution and change in the optical absorption of BC following particle aging and transport. The T_{OC}/D_{BC} ratio determines whether BC particles can be redistributed into organic coatings from inorganic salt cores. When the organic coating is non-absorbing, the light absorption of internally mixed particles containing one and two BC reduces by 28–34% following the BC redistribution. Further, the radiative absorption of BC in the background air is overestimated by ~18% in most models that assume internally mixed BC aerosols to be the core-shell model.

vitrobot mark IV humidity chamber under the settled RH (e.g., $75 \pm 2\%$, $86 \pm 2\%$, and $95 \pm 2\%$) at 296 K for 10 min (Supplementary Fig. 7). After that, the samples were quickly transferred from the vitrobot mark IV humidity chamber into a container with liquid ethane and liquid nitrogen instantaneously cooling to ~ 104 K (Supplementary Fig. 7). Aerosols in the samples were immediately frozen in the cold container so that we can move the frozen sample to the cryo-TEM holder. Further, we observed the real morphology, sizes, and mixing structures of individual particles at different RH (Supplementary Fig. 7).

To correct particle size and organic coating thickness (T_{OC}), individual particles collected on silicon wafers were analyzed using atomic force microscopy (AFM, Dimension Icon, USA). On the basis of TEM observations, we selected four typical samples collected at two background sites for AFM analysis. A total of 113 particles at the rural site and 32 particles at the mountain site were analyzed. In this study, an image analysis software (NanoScope Analysis, Bruker, Germany) was used to automatically analyze the bearing areas and bearing volumes of particles in AFM images. The ECDs and equivalent sphere diameters (ESDs) of individual particles in AFM images were further calculated according to the following two equations:

$$d = \sqrt{\frac{3A}{\pi}} \quad (1)$$

$$D = \sqrt[3]{\frac{6V}{\pi}} \quad (2)$$

where d is ECD; D is ESD; A is bearing area; V is bearing volume.

There is a good linear relationship between the ECD and ESD of particles (Supplementary Fig. 14). Based on the linear correlation, we further calculated ESDs of particles at the sampling sites. T_{OC} was also obtained according to the following equation:

$$T_{OC} = (ESD_p - ESD_c)/2 \quad (3)$$

where ESD_p is ESD of the individual particle; ESD_c is ESD of the inorganic salt core.

Laboratory experiments of BC redistribution. Dicarboxylic acid and ammonium sulfate are among the most abundant organic and inorganic species in the atmosphere. Laboratory results have suggested that liquid-liquid phase separation (LLPS) can occur in the mixtures of 3,3-dimethylglutaric acid (a dicarboxylic acid) and ammonium sulfate³⁸. Two ternary solutions of 3,3-dimethylglutaric acid/ammonium sulfate/deionized water (organic-to-inorganic dry mass ratio (OIR) = 1:4 and OIR = 7:1) mixed with commercial BC (> 99.9% purity from Alfa Aesar, CAS number: 1333-86-4, mass fraction in the solution of $\sim 0.1\%$) were prepared in the laboratory. The concentrations of 3,3-dimethylglutaric acid and ammonium sulfate were 0.08 mol L^{-1} and 0.38 mol L^{-1} in the solution with OIR = 1:4 and 0.31 mol L^{-1} and 0.05 mol L^{-1} in the solution with OIR = 7:1. The pH values of solutions with OIR = 1:4 and 7:1 were 2.83 and 2.29. The suspensions containing BC were then subjected to ultrasonic oscillation for 30 min to ensure that the BC was diffusely suspended in the solutions (Supplementary Fig. 9). We then generated individual organic/inorganic/BC mixed aerosols through an aerosol atomizer (Badger, USA) that can generate particles of 200–20000 nm. The aerosol atomizer has been successfully applied to generate different types of individual particles (e.g., $(\text{NH}_4)_2\text{SO}_4$ and NaCl)^{36,37}. The generated organic/inorganic/BC mixed aerosols were deposited on TEM grids to observe the mixing structure and distribution of BC through TEM analysis. We found that the morphology and mixing state of the laboratory-generated BC-containing particles were same as BC-containing particles in the atmosphere (Supplementary Figs. 8 and 10a, b). Therefore, the particles generated from the suspensions can represent typical BC-containing particles in the ambient air.

Optical calculations of BC-containing particles. We used the DDSCAT 7.3 program for the discrete dipole approximation (DDA) calculation at an incident light wavelength (λ) of 550 nm⁵⁰. A novel Electron-Microscope-to-BC-Simulation (EMBS) tool was applied to construct the shape models of BC-containing particles²⁴. The EMBS facilitates to flexibly construct various shape models of BC-containing particles with complex mixing structures and morphology, which can be applied in DDSCAT 7.3 to calculate optical properties of BC-containing particles. In this study, the absorption enhancement (E_{abs}) of BC-in-Icore (BC occurring in inorganic salt core) particles and BC-in-Ocoating (BC occurring in organic coating) particles relative to the BC core in the background air was calculated using EMBS and DDSCAT 7.3. Because BC particles are mainly aged in the background air, the fractal dimension of BC was assumed as 2.16⁵¹. In the optical calculation, the total volumes of BC-in-Icore and BC-in-Ocoating particles remain unchanged. For the BC-in-Icore particles with organic coatings (phase-separated core-shell model), the sulfate core diameters are 432 nm (rural background air) and 538 nm (mountain background air), and the organic coating thicknesses are 81 nm and 80 nm (Supplementary Fig. 13). For the BC-in-Icore particles without organic coatings (basic core-shell model), the sulfate diameters are 594 nm (rural) and 698 nm (mountain), which are equal to the diameters of the phase-separated core-shell model. For BC-in-Ocoating particles (redistributed model), the diameters of the whole particle are also 594 nm and 698 nm. Meanwhile, the total volume of BC particles is constant (single BC diameter: 116 nm for rural air and 126 nm for

mountain air) (Supplementary Fig. 13). The basic core-shell model was classified into two types: BC in the center and in the eccentric area of individual particles. The phase-separated core-shell model was also classified into two types: BC in the center and touching the interface between the organic and inorganic species of individual particles. Here three types of models containing one and two BC were considered and the organic coating was assumed to be non-absorbing in the optical calculation (Fig. 5). Supplementary Table 3 shows the exact coordinate of BC within different individual BC-containing particle models. DDA is completely flexible for the geometry of the object particle, but the inter dipole separation d must abide by the relationship $|m|kd < 0.5$, where m is the refractive index of the particle and $k = 2\pi/\lambda$. The dipole size in this study is much smaller than the monomer size to minimize the uncertainty in DDA. We used 1000 incident light angles for each particle, assuming that the particles are randomly oriented in the atmosphere. The refractive indices for BC, sulfate, and non-absorbing organic coating are $1.85 + 0.71i^{52}$, $1.53 + 0i^{53}$, and $1.65 + 0i^{47}$, respectively. More details on the DDA calculation can be found in Wang et al.²⁴.

Data availability

The observation, laboratory experiment, and simulation data that support the main findings of this study are available at figshare data publisher (<https://doi.org/10.6084/m9.figshare.14564388.v3>). The original TEM and cryo-TEM images used in this study can not be uploaded due to large data storage and can be available upon request from the corresponding author.

Code availability

The source code of the DDSCAT 7.3 can be available at <http://ddscat.wikidot.com/>. The code of the EMBS is available at <https://doi.org/10.6084/m9.figshare.13606304>.

Received: 7 December 2021; Accepted: 16 May 2022;

Published online: 02 June 2022

References

- Bond, T. C. et al. Bounding the role of black carbon in the climate system: A scientific assessment. *J. Geophys. Res. Atmos.* **118**, 5380–5552 (2013).
- Seinfeld, J. Black carbon and brown clouds. *Nat. Geosci.* **1**, 15–16 (2008).
- Jacobson, M. Z. Strong radiative heating due to the mixing state of black carbon in atmospheric aerosols. *Nature* **409**, 695–697 (2001).
- Cappa, C. D. et al. Radiative absorption enhancements due to the mixing state of atmospheric Black carbon. *Science* **337**, 1078–1081 (2012).
- Menon, S., Hansen, J., Nazarenko, L. & Luo, Y. Climate effects of black carbon aerosols in China and India. *Science* **297**, 2250–2253 (2002).
- Ding, A. J. et al. Enhanced haze pollution by black carbon in megacities in China. *Geophys. Res. Lett.* **43**, 2873–2879 (2016).
- Ramanathan, V. & Carmichael, G. Global and regional climate changes due to black carbon. *Nat. Geosci.* **1**, 221–227 (2008).
- Wang, Q. et al. Physicochemical characteristics of black carbon aerosol and its radiative impact in a polluted urban area of China. *J. Geophys. Res.-Atmos.* **121**, 12505–12519 (2016).
- Zhou, C., Zhang, H., Zhao, S. & Li, J. Simulated effects of internal mixing of anthropogenic aerosols on the aerosol–radiation interaction and global temperature. *Int. J. Climatol.* **37**, 972–986 (2017).
- Peng, J. et al. Markedly enhanced absorption and direct radiative forcing of black carbon under polluted urban environments. *Proc. Natl. Acad. Sci. U.S.A.* **113**, 4266–4271 (2016).
- He, C. et al. Variation of the radiative properties during black carbon aging: Theoretical and experimental intercomparison. *Atmos. Chem. Phys.* **15**, 11967–11980 (2015).
- Zhang, X., Mao, M., Yin, Y. & Tang, S. The absorption Ångström exponent of black carbon with brown coatings: Effects of aerosol microphysics and parameterization. *Atmos. Chem. Phys.* **20**, 9701–9711 (2020).
- Li, K. et al. Temporal variations in the hygroscopicity and mixing state of black carbon aerosols in a polluted megacity area. *Atmos. Chem. Phys.* **18**, 15201–15218 (2018).
- Cheng, Y. et al. Size-resolved measurement of the mixing state of soot in the megacity Beijing, China: Diurnal cycle, aging and parameterization. *Atmos. Chem. Phys.* **12**, 4477–4491 (2012).
- Wang, Y. et al. Nonlinear enhancement of radiative absorption by black carbon in response to particle mixing structure. *Geophys. Res. Lett.* **48**, e2021GL096437 (2021).
- Fierce, L. et al. Radiative absorption enhancements by black carbon controlled by particle-to-particle heterogeneity in composition. *Proc. Natl. Acad. Sci. U.S.A.* **117**, 5196–5203 (2020).

17. Riemer, N., Ault, A. P., West, M., Craig, R. L. & Curtis, J. H. Aerosol mixing state: Measurements, modeling, and impacts. *Rev. Geophys.* **57**, 187–249 (2019).
18. Scarnato, B. V., Vahidinia, S., Richard, D. T. & Kirchstetter, T. W. Effects of internal mixing and aggregate morphology on optical properties of black carbon using a discrete dipole approximation model. *Atmos. Chem. Phys.* **13**, 5089–5101 (2013).
19. Liu, S. et al. Enhanced light absorption by mixed source black and brown carbon particles in UK winter. *Nat. Commun.* **6**, 8435 (2015).
20. Flanner, M. G., Zender, C. S., Randerson, J. T. & Rasch, P. J. Present-day climate forcing and response from black carbon in snow. *J. Geophys. Res. Atmos.* **112**, D11202 (2007).
21. Liu, D. et al. Black-carbon absorption enhancement in the atmosphere determined by particle mixing state. *Nat. Geosci.* **10**, 184–188 (2017).
22. Wu, Y. et al. Light absorption enhancement of black carbon aerosol constrained by particle morphology. *Environ. Sci. Technol.* **52**, 6912–6919 (2018).
23. Luo, J. et al. Optical modeling of black carbon with different coating materials: The effect of coating configurations. *J. Geophys. Res. Atmos.* **124**, 13230–13253 (2019).
24. Wang, Y. et al. Constructing shapes and mixing structures of black carbon particles with applications to optical calculations. *J. Geophys. Res. Atmos.* **126**, e2021JD034620 (2021).
25. McMeeking, G. R. et al. Impacts of nonrefractory material on light absorption by aerosols emitted from biomass burning. *J. Geophys. Res. Atmos.* **119**, 12,272–12,286 (2014).
26. Adachi, K., Chung, S. H. & Buseck, P. R. Shapes of soot aerosol particles and implications for their effects on climate. *J. Geophys. Res. Atmos.* **115**, D15206 (2010).
27. Lee, A. K. Y. et al. Influences of primary emission and secondary coating formation on the particle diversity and mixing state of black carbon particles. *Environ. Sci. Technol.* **53**, 9429–9438 (2019).
28. China, S. et al. Morphology and mixing state of aged soot particles at a remote marine free troposphere site: Implications for optical properties. *Geophys. Res. Lett.* **42**, 1243–1250 (2015).
29. Zhang, R. et al. Variability in morphology, hygroscopicity, and optical properties of soot aerosols during atmospheric processing. *Proc. Natl. Acad. Sci. U.S.A.* **105**, 10291–10296 (2008).
30. Liu, F., Wong, C., Snelling, D. R. & Smallwood, G. J. Investigation of absorption and scattering properties of soot aggregates of different fractal dimension at 532nm using RDG and GMM. *Aerosol Sci. Tech.* **47**, 1393–1405 (2013).
31. Brunamonti, S., Krieger, U. K., Marcolli, C. & Peter, T. Redistribution of black carbon in aerosol particles undergoing liquid-liquid phase separation. *Geophys. Res. Lett.* **42**, 2532–2539 (2015).
32. Moffet, R. C. et al. Morphology and mixing of black carbon particles collected in central California during the CARES field study. *Atmos. Chem. Phys.* **16**, 14515–14525 (2016).
33. Li, W. et al. A conceptual framework for mixing structures in individual aerosol particles. *J. Geophys. Res. Atmos.* **121**, 13784–13798 (2016).
34. You, Y. et al. Images reveal that atmospheric particles can undergo liquid-liquid phase separations. *Proc. Natl. Acad. Sci. U.S.A.* **109**, 13188–13193 (2012).
35. O'Brien, R. E. et al. Liquid-liquid phase separation in aerosol particles: Imaging at the nanometer scale. *Environ. Sci. Technol.* **49**, 4995–5002 (2015).
36. Li, W. et al. Microscopic evidence for phase separation of organic species and inorganic salts in fine ambient aerosol particles. *Environ. Sci. Technol.* **55**, 2234–2242 (2021).
37. Li, W. et al. Organic coating reduces hygroscopic growth of phase-separated aerosol particles. *Environ. Sci. Technol.* **55**, 16339–16346 (2021).
38. Song, M., Marcolli, C., Krieger, U. K., Zuend, A. & Peter, T. Liquid-liquid phase separation in aerosol particles: Dependence on O:C, organic functionalities, and compositional complexity. *Geophys. Res. Lett.* **39**, L19801 (2012).
39. Wang, H. Formation of nascent soot and other condensed-phase materials in flames. *P. Combust. Inst.* **33**, 41–67 (2011).
40. Adler, G., Riziq, A. A., Erlick, C. & Rudich, Y. Effect of intrinsic organic carbon on the optical properties of fresh diesel soot. *Proc. Natl. Acad. Sci. U.S.A.* **107**, 6699–6704 (2010).
41. Long, C. M., Nascarella, M. A. & Valberg, P. A. Carbon black vs. black carbon and other airborne materials containing elemental carbon: Physical and chemical distinctions. *Environ. Pollut.* **181**, 271–286 (2013).
42. Johansson, K. O., Head-Gordon, M. P., Schrader, P. E., Wilson, K. R. & Michelsen, H. A. Resonance-stabilized hydrocarbon-radical chain reactions may explain soot inception and growth. *Science* **361**, 997–1000 (2018).
43. Buseck, P. R., Adachi, K., Gelencsér, A., Tompa, É. & Pósfai, M. N-Soot: A material-based term for strongly light-absorbing carbonaceous particles. *Aerosol Sci. Tech.* **48**, 777–788 (2014).
44. Clague, A. D. H., Donnet, J. B., Wang, T. K. & Peng, J. C. M. A comparison of diesel engine soot with carbon black. *Carbon* **37**, 1553–1565 (1999).
45. Li, M. et al. Role of elemental carbon in the photochemical aging of soot. *Proc. Natl. Acad. Sci. U.S.A.* **115**, 7717–7722 (2018).
46. Mishchenko, M. I., Liu, L., Cairns, B. & Mackowski, D. W. Optics of water cloud droplets mixed with black-carbon aerosols. *Opt. Lett.* **39**, 2607–2610 (2014).
47. Feng, Y., Ramanathan, V. & Kotamarthi, V. R. Brown carbon: A significant atmospheric absorber of solar radiation? *Atmos. Chem. Phys.* **13**, 8607–8621 (2013).
48. Tuccella, P., Curci, G., Pitari, G., Lee, S. & Jo, D. S. Direct radiative effect of absorbing aerosols: Sensitivity to mixing state, brown carbon, and soil dust refractive index and shape. *J. Geophys. Res. Atmos.* **125**, e2019JD030967 (2020).
49. Xu, L. et al. Variation in concentration and sources of black carbon in a megacity of China during the COVID-19 pandemic. *Geophys. Res. Lett.* **47**, e2020GL090444 (2020).
50. Draine, B. T. & Flatau, P. J. Discrete-dipole approximation for scattering calculations. *J. Opt. Soc. Am. A* **11**, 1491–1499 (1994).
51. Wang, Y. et al. Fractal dimensions and mixing structures of soot particles during atmospheric processing. *Environ. Sci. Technol. Lett.* **4**, 487–493 (2017).
52. Bond, T. C. & Bergstrom, R. W. Light absorption by carbonaceous particles: An investigative review. *Aerosol Sci. Tech.* **40**, 27–67 (2006).
53. Worringer, A., Ebert, M., Trautmann, T., Weinbruch, S. & Helas, G. Optical properties of internally mixed ammonium sulfate and soot particles—a study of individual aerosol particles and ambient aerosol populations. *Appl. Optics* **47**, 3835–3845 (2008).

Acknowledgements

Cryo-TEM characterization was conducted at the Center of Cryo-Electron Microscopy, Zhejiang University, with the assistance of Lingyun Wu. We appreciate Peter Hyde's comments and proofreading. We thank Xiaokun Ding for his assistance in the HAADF-STEM analysis. We thank Gang Li for his assistance in collecting the samples. This work was funded by the National Natural Science Foundation of China (42075096 and 91844301) and Zhejiang Provincial Natural Science Foundation of China (LZ19D050001).

Author contributions

W.L., J.Z., and Y.W. conceived the study, led the overall scientific questions, and wrote the manuscript. The field campaigns were organized and supervised by W.L., J.Z. and L.L. made the laboratory experiments. Y.W. made the modelling studies. W.L., J.Z., and X.T. made the cryo-TEM analysis. J.Z. and W.L. contributed the data analysis. Y.X. and L.R. provided the hourly measurement data of pollutants at the mountain background site. Z.S. interpreted the results and contributed to the experimental design. Z.S., Y.Z., J.J., D.L., M.H., L.S., J.C., S.T.M., and X.Z. reviewed and commented on the paper.

Competing interests

The authors declare no competing interests.

Additional information

Supplementary information The online version contains supplementary material available at <https://doi.org/10.1038/s43247-022-00462-1>.

Correspondence and requests for materials should be addressed to Weijun Li.

Peer review information *Communications Earth & Environment* thanks the anonymous reviewers for their contribution to the peer review of this work. Primary Handling Editors: Kerstin Schepanski and Clare Davis. Peer reviewer reports are available.

Reprints and permission information is available at <http://www.nature.com/reprints>

Publisher's note Springer Nature remains neutral with regard to jurisdictional claims in published maps and institutional affiliations.



Open Access This article is licensed under a Creative Commons Attribution 4.0 International License, which permits use, sharing, adaptation, distribution and reproduction in any medium or format, as long as you give appropriate credit to the original author(s) and the source, provide a link to the Creative Commons license, and indicate if changes were made. The images or other third party material in this article are included in the article's Creative Commons license, unless indicated otherwise in a credit line to the material. If material is not included in the article's Creative Commons license and your intended use is not permitted by statutory regulation or exceeds the permitted use, you will need to obtain permission directly from the copyright holder. To view a copy of this license, visit <http://creativecommons.org/licenses/by/4.0/>.

© The Author(s) 2022